

Transformed Low-rank Model for Line Pattern Noise Removal

Yi Chang, Luxin Yan*, Sheng Zhong

National Key Laboratory of Science and Technology on Multispectral Information Processing
School of Automation, Huazhong University of Science and Technology, China

{yichang, yanluxin, zhongsheng}@hust.edu.cn

Abstract

This paper addresses the problem of line pattern noise removal from a **single** image, such as rain streak, hyperspectral stripe and so on. Most of the previous methods model the line pattern noise in original image domain, which fail to **explicitly** exploit the directional characteristic, thus resulting in a redundant subspace with poor representation ability for those line pattern noise. To achieve a compact subspace for the line pattern structure, in this work, we incorporate a transformation into the image decomposition model so that maps the input image to a domain where the line pattern appearance has an extremely distinct low-rank structure, which naturally allows us to enforce a low-rank prior to extract the line pattern streak/stripe from the noisy image. Moreover, the random noise is usually mixed up with the line pattern noise, which makes the challenging problem much more difficult. While previous methods resort to the spectral or temporal correlation of the multi-images, we give a detailed analysis between the noisy and clean image in both local gradient and nonlocal domain, and propose a compositional directional total variational and low-rank prior for the image layer; thus to simultaneously accommodate both types of noise. The proposed method has been evaluated on two different tasks, including remote sensing image mixed random-stripe noise removal and rain streak removal, all of which obtain very impressive performances.

1. Introduction

The random noise removal problem has attracted much of the attention and progressed rapidly during the past decades [1, 26, 10, 39, 2, 15, 29, 9, 33, 38, 7]. By contrast, the field of line pattern structural noise removal problem has received less attention as of today despite their abundant application in the real world, such as the stripe noise in remote sensing images [27, 5, 37, 4, 32], the rain streak in natural images [14, 19, 8, 23, 21], the nonuniformity in images acquired by focal plane arrays [25], ringing artifact

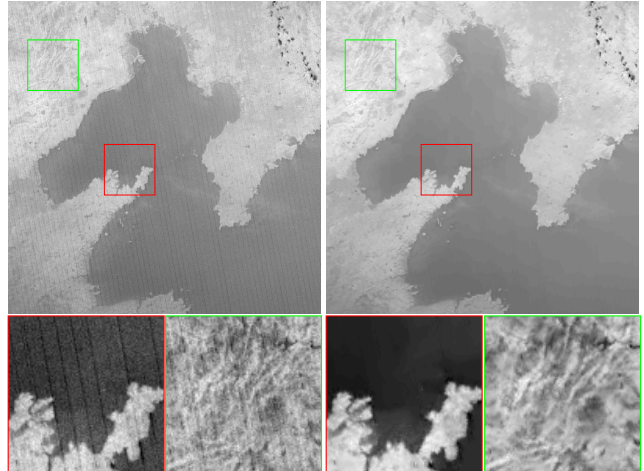


Figure 1. An example on the challenging issue: line pattern noise with random noise removal via a single image. The left is the degraded image, the right shows the proposed result with noise-free background and clear texture.

in medical images [11, 17], to name a few. Unfortunately, these different communities have seldom exchanged ideas with each other. In this work, we summarise them as the line pattern noise removal problem, and make an attempt to settle this problem as well as the random noise. Figure 1 shows one example of a georeference MODIS image contaminated with mixed stripe and random noise, where our method is able to recover the clean background and texture in single image.

Given a single line pattern noisy image, traditional methods solve this issue via the image denoising strategy by enforcing various prior knowledge on the image, ignoring to model the line pattern noise in a principal manner [18, 20]. Consequently, the resulting image is either over-smooth or containing residual line pattern noise. Another research direction utilizes the image decomposition framework by treating the image component and line pattern structural noise component equally [19, 23, 21, 6]. Such a simple improvement gives this problem a meaningful interpreta-

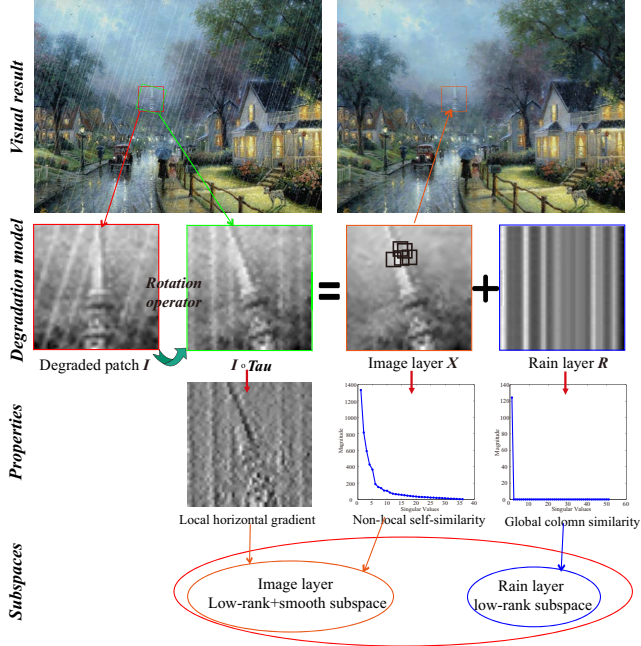


Figure 2. Overview of the proposed method. In the second row, the input rain image is transformed to the domain where the rain streak has strictly vertical appearance. In the transformed domain, the image layer and rain streak layer has distinct properties (third row) and can be projected to different subspaces (fourth row). Thus, the rain and image background are separated from each other, and the result of proposed method is visual pleasure (first row, right part).

tion. The intuition behind these state-of-the-art methods is to make the two components lie on two different subspaces. Thus, the key of the problem is transferred to how to construct two reasonable measurements to differ the image component from the line pattern component.

The pioneer work [19] utilizes the widely used sparse coding based on morphological component analysis and learns two dictionaries: “rain” dictionary and “non-rain” dictionary. Further, the sophisticated Gaussian mixture models (GMMs) is introduced by Li *et al.* [21] for both the rain layer and image layer with impressive performance, which can be regarded as a fine-grained multi-dictionaries version of [19]. The authors [23] go further by borrowing the concept of discriminative sparse coding to additionally regularize the two learned dictionaries with mutual exclusivity property, thus making estimated rain and image layer distinguishable. However, an inevitable difficulty in previous methods is that the ambiguity between rain and image dictionary. Even learning with a more compact dictionary [23], the problem still remains due to inherent ambiguity between line pattern noise and image structures in original image domain. Moreover, they fail to **explicitly** exploit the directional characteristic of line pattern noise, resulting in a redundant subspace with weak representation ability.

To avoid these limitations, we offer a new perspective to model the line pattern structural noise in the transformed domain with the low-rank subspace constraint, not the original image domain. The advantage of our method is two-folds. First, in the transformed domain, the line pattern noise show significantly vertical appearance, which facilitate us to differ it from the image content more easily. Second, in the transformed domain, the subspace belong to the rain layer is usually very compact. For example, we can see that in Fig. 2, the rotated rain image can be approximately equal to a rank 1 matrix¹. Motivated by this observation, a simple yet effective transformed image decomposition model is proposed to explicitly accommodate the structural and directional line pattern with low-rank prior in compact and representative manner.

In addition, we also take the random noise into consideration, which is usually associated with the line pattern noise in real situation [4, 27]. Previous works resort to the additional multispectral of temporal information to solve this challenging problem [25, 34, 5, 4, 16, 32]. To distinguish the image background from the line pattern and random noise, our start point is from the single image. To this end, we analyse both the influence of random noise and line pattern noise on the clean image. In the transformed domain, we discover that the line pattern noise change the statistical distribution of horizontal gradient obviously, while the vertical gradient are less changed. This inspires us to utilize the directional total variational to capture this discrepancy in the image gradient domain, so as to separate the line pattern noise from the clean image in the transformed domain. Also, the non-local self-similarity based low-rank prior is employed to remove the random noise as well known. We show that the compositional directional total variational and low-rank prior is complementary to each other and very effective for mixed noise removal.

The contributions of this work are as follows: 1) We explicitly utilize the directional characteristic of the line pattern, and model it via the rotated image decomposition framework, which benefits us to reveal the low-rank subspace of the line pattern noise in the transformation domain with a more compact manner; 2) We exploit both the local and nonlocal sparsity of the image layer to accommodate the mixed noise case, and a compositional directional total variational and low-rank prior is proposed to separate the image layer from the noise; 3) The proposed method has been applied on rain streak removal and hyperspectral stripe removal tasks with impressive performance. Our single image based method is even superior to the state-of-the-art multispectral image based methods in some cases.

¹Our method is applied in local patch way, not on the whole image, so that the low-rank assumption of the transformed rain patch can be satisfied. We perform the SVD on the constructed low-rank matrix. The horizontal axis represents the index of its singular value, and the vertical axis stands for the corresponding magnitude of the singular value.

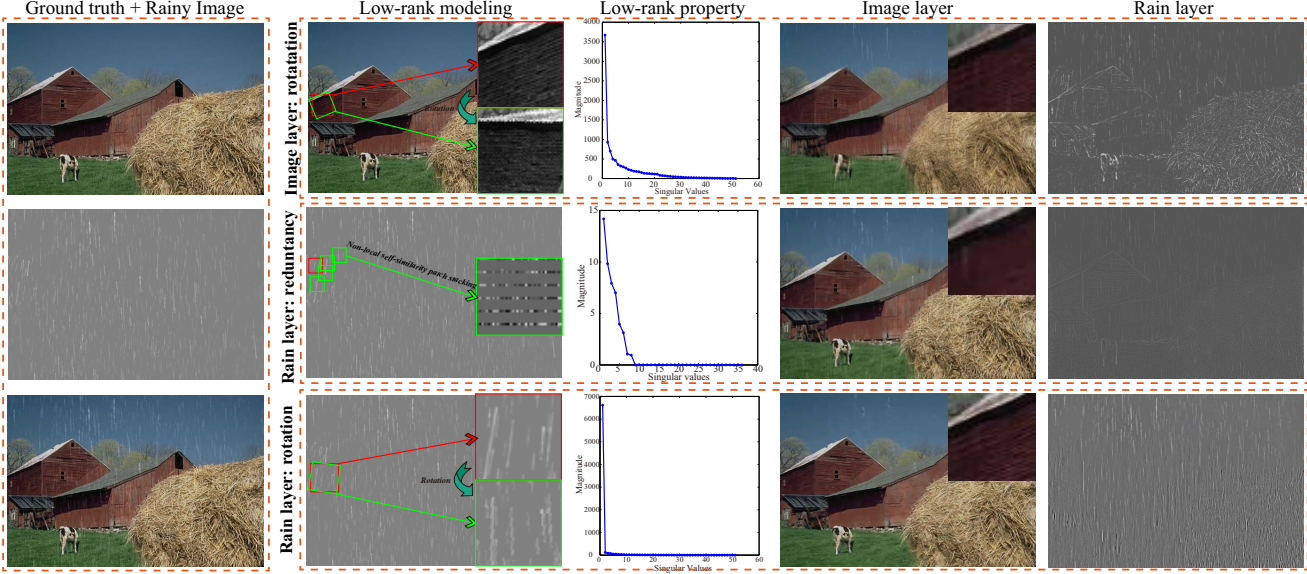


Figure 3. Illustration of the effectiveness of the proposed transformed low-rank prior for rain streak and low-rank modeling comparison between our and two representative methods. The first and second rows illustrate the image layer transformed [30] and rain streak non-local self-similarity based low-rank models [8], respectively. The third row shows our rain streak layer transformed based low-rank model. Our method preserves the image texture better (lines of image layer in zoom region) and the rain layer contains only the streak component.

2. Related work

Rotated degradation model: It has been shown that an image patch has more distinct low-rank property in the transformed domain than that of the original space [36], which has been widely used in image alignment [28], super-resolution [12], and non-pointwise noise removal [30]. Our starting point to capture the low-rank property in transformed domain is in line with them, while we take a step from the opposite direction by regularizing the line pattern layer with the low-rank, not on the background image layer. That is because the low-rankness of line pattern layer is much stronger than that of background layer (section 3.2). To our knowledge, this is the first method to use rotated degradation model for line pattern noise removal.

Line pattern modeling: The existing methods differ in the regularization they used, in which the dictionary learning [19, 23], GMM [21], and low-rank [8, 6] have been introduced for line pattern noise modeling. However, the line pattern noise has distinctly directional property with simple structure in a local appearance, while previous methods fail to capture its intrinsic compact subspace. In this work, we argue that the low-rank property of the transformed domain is much more superior to that of the others for compact representation of the line pattern noise (section 3.2).

Image layer modeling: For most of existing single image based methods [19, 23, 21], the philosophy is to treat the image layer and line pattern layer equally with the same constraint. However, we hold the viewpoint of **common but different**

importance between the two layers. The main reason is that although the line pattern noise has structural appearance, the image background has much more abundant structural information with various direction and scale. In this work, by giving a detailed analysis of the local and non-local discrepancy between original and degraded image layer, we propose a compositional directional total variational and low-rank prior for better modeling the image structure (section 3.3).

Mixed noise removal: In real applications, such as the hyperspectral image, the random noise and stripe noise always coexist [27, 34, 29, 25, 5, 4, 16, 32]. For this challenging problem, existing methods mainly rely on the spectral or temporal information with strong assumption that image sequences are aligned. Previous single image de-raining methods [19, 23, 21] also cannot solve this issue well. They model the image layer inadequately and are sensitive to the random noise. In our work, we sidestep the requirement and settle the problem in single image via modeling the image layer more elaborately (section 3.3).

3. Our method

3.1. Rotated degradation model

Most of the existing line pattern noise removal methods model the degradation procedure as a linear additive composition [19, 8, 27, 30, 34, 4, 37, 6, 21, 16], assuming that the degraded image $\mathbf{I} \in \mathbb{R}^{M \times N}$ is composed by two layers, image layer \mathbf{X} and line pattern noise layer \mathbf{R} , as follows:

$\mathbf{I} = \mathbf{X} + \mathbf{R}$. Thus, this ill-posed problem can be transferred to estimate clean \mathbf{X} and \mathbf{R} from degraded image \mathbf{I} with proper constraints. However, the significant features may not be captured in the original image domain [36, 12], especially for the line pattern noise with distinct direction characteristic. To explicitly utilize this most important information, we propose to model the line pattern noise degradation procedure with a rotation operator:

$$\mathbf{I} \circ \tau = \mathbf{X} + \mathbf{R} + \mathbf{N}, \quad (1)$$

where τ is an affine transform to align the line pattern noise vertically (Fig. 2), and \mathbf{N} is the random noise. And we differ from previous transformed models, in which previous works seldom consider the random noise factor.

3.2. Line pattern modeling

In this section, we explain why low-rank property in transformed domain for the line pattern noise is more superior to that of previous methods. To illustrate this, in Fig. 3, we provide three representative examples in which the constructed low-rank matrixes differ from each other. Three representative ways to form the low-rank matrix are shown from the first row to the third row: rotate the image patch, redundancy in rain patch, rotate the rain patch. It is clearly observed that singular values of the constructed low-rank matrix exhibit sparsity with different degrees.

Compared with the rotated rain layer, the intrinsic subspace of the rotated image layer (First row in Fig. 3, approximately rank 30) is much more redundant. This can be naturally understood that the image layer has much complex structural information than that of rain layer. Also, the redundancy relationship (Second row in Fig. 3, approximately rank 8) can hardly capture the precise directional properties of the rain streak, thus cannot reflect the underlying subspace of the rain streak. In contrast, the low-rank subspace of our rotated rain layer (Third row in Fig. 3, approximately rank 1) is most compact and representative.

Consequently, we can observe that the corresponding estimated image layer and rain streak layer strongly associate with their low-rank properties. All these results highlight the fact the low-rank constraint for the rotated line pattern noise is the most compact manner to represent its directional and structural properties, and motivate us to leverage the low-rank prior for the line pattern noise.

3.3. Image layer modeling

Developing sophisticated image priors has been the focus of much image processing in the past decades, with many significant successes. However, previous methods utilize the conventional total variational [8, 6, 21], GMM [21] prior as the line pattern noise equally. On one hand, they overemphasize the importance of the line pattern layer and employ the same constraints for both the image layer and the line pattern layer, overlooking the fact that image

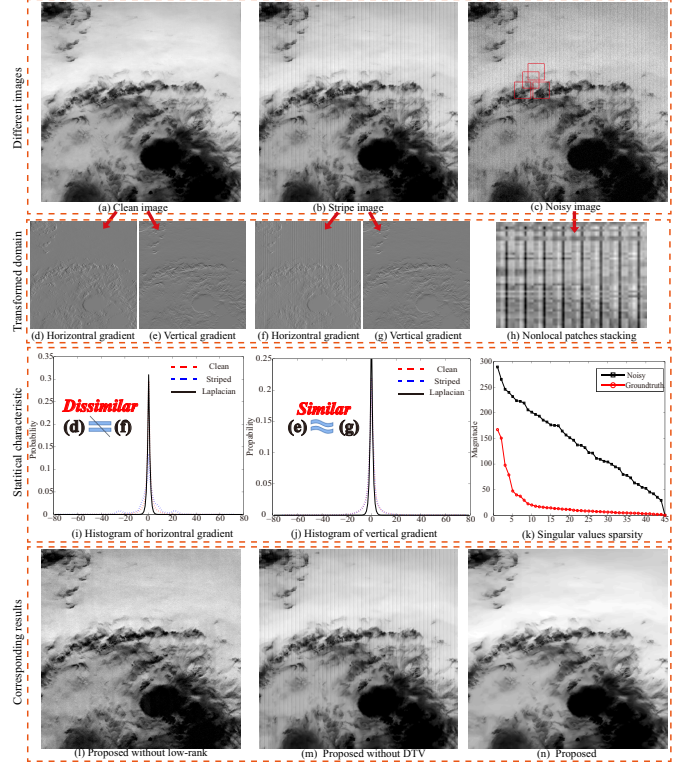


Figure 4. Effectiveness of local based directional total variational for stripe noise and non-local based low-rank for random noise. We analyze the gradient and low-rank property between the clean and both noise degraded image in transformed domain (second row and third row). Please refer to section 3.3 for detail.

layer has much more abundant structures; On the other hand, they do not figure out how the line pattern and random noise influence the statistical characteristic of the image layer exactly, which may result in poor removal results.

To overcome these limitations, we firstly analyze the gradient statistical distribution before and after stripe noise degraded. As shown in Fig. 4, we can observe that in the rotated image domain, the horizontal gradient map between Fig. 4(d) and 4(f) changes a lot, while the vertical gradient map between Fig. 4(e) and 4(g) is similar. Further, we plot their corresponding gradient histograms in Fig. 4(i) and 4(j). We observe that the gradient distribution of Fig. 4(e) and Fig. 4(g) is almost the same [shown in Fig. 4(j)], and the gradient distribution of Fig. 4(e) and 4(g) is absolutely different [shown in Fig. 4(i)].

Such an observation is not surprising, since the stripe line has significantly directional feature. That is to say it increases the gradient variation across the stripe line direction (the horizontal direction) while has less influence along the stripe line. This motivate us to introduce the directional total variational [5], so as to smooth the horizontal gradient and preserve the vertical gradient.

As for the random noise, in Fig. 4(k), we can see that the random noise influences the low-rank property of the non-local stacked matrix. It is natural for us to introduce the low-rank prior to our image modeling. Thus, the local gradient and nonlocal low-rank prior are proposed to jointly represent the image structure.

Further, we demonstrate that the compositional directional total variational and low-rank prior is complementary to each other and very effective for mixed noise problem, in Fig. 4(l) to 4(n). We can see that directional total variational is particularly effective to suppress the stripe noise [Fig. 4(l)], while low-rank is particularly effective to the random noise [Fig. 4(m)]. By combining both constraints into the rotated image decomposition framework, our method iteratively restores the clear image and line noise component [Fig. 4(n)]. Note that, the contribution of this work is not about the conventional low-rank or TV priors for image modeling but why we combine them for mixed noise removal and how it differs from the line pattern modeling.

3.4. Transformed low-rank recovery model

Putting all terms together leads to the transformed low-rank (TLR) image recovery model:

$$\begin{aligned} & \min_{X, R, A_i, \tau} \|R\|_* + \lambda_1 (\|\nabla_x X\|_1 + \rho \|\nabla_y (I \circ \tau - X)\|_1) \\ & + \lambda_2 \sum_i (\|A_i\|_* + \mu \|\hat{P}_i \text{Vec}(X) - A_i\|_F^2) \quad \text{s.t. } I \circ \tau = X + R, \end{aligned} \quad (2)$$

where $\lambda_1, \lambda_2, \rho, \mu$ are the tradeoff parameters, $\|\bullet\|_*$ represents the nuclear norm for the convex surrogate functional of low-rank constraint, ∇_x and ∇_y denote the horizontal and vertical derivative operator, respectively, $A_i \in R^{p^2 \times m}$ in (2) is the clear low-rank matrix, where p is the size of the small key patch, m is the total number of the similar patches, and \hat{P}_i contains m matrixes ($p^2 \times MN$) that extracts the small patch from the larger image patch $\text{Vec}(X) \in R^{MN \times 1}$.

Our model unifies the image transformation, image denoising, and line pattern noise removal in a framework. The basic idea of the model is that in the transformed image domain, the image subspace could be effectively regularized by the compositional directional total variational and low-rank prior, and meanwhile the low-rank prior identifies the line pattern noise subspace. On one hand, a less line pattern noise image has positive impact on the non-local similar patch searching, thus facilitating the random noise removal; on the other hand, a less random noise image would undoubtedly boost the line pattern extraction.

3.5. Optimization

Due to the nonlinear property of the measurement constraint in (2), a common technique to overcome this difficulty is to linearize the constraint around the current estimate and iterate as follows: $I \circ \tau + \nabla I \Delta \tau = X + R$ [36], where ∇I is the Jacobian (derivatives of the image with

respect to the transformation parameters). Thus, our final linearized problem is a convex program with respective to four variables $\Delta \tau, X, R, A_i$, can be converted into four simpler sub-problems via alternating minimization with distinct physical meanings.

1) Update for R : Line pattern noise estimation. In this subproblem, we fix the other variables and optimize R :

$$\hat{R} = \arg \min_R \|R\|_* + \frac{\alpha}{2} \|I \circ \tau + \nabla I \Delta \tau - X - R - \frac{J}{\alpha}\|_F^2, \quad (3)$$

where J and α is the Lagrangian multiplier and constant value, respectively, so as to convert the constrained problem (2) into its unconstrained subproblem (3). Equation (3) is a typical low-rank matrix approximation problem which has a closed-form solution and can be easily solved by the singular values thresholding algorithm [3].

2) Update for A_i : Image denoising. By ignoring terms independent of A_i , we obtain following subproblem:

$$\hat{A}_i = \arg \min_{A_i} \|A_i\|_* + \mu \|\hat{P}_i \text{Vec}(X) - A_i\|_F^2, \quad (4)$$

which also can be solved by conventional singular values thresholding algorithm [3]. Instead of the conventional nuclear norm, we introduce the weighted nuclear norm from [15] to improve the denoising performance, since this reweighting strategy can adaptively accommodate to the varying noise level.

3) Update for X : Image restoration. Similarly, dropping out the irrelevant variables, we can recover the desired image by solving the following subproblem:

$$\begin{aligned} \hat{X} = & \arg \min_X \lambda_1 (\|\nabla_x X\|_1 + \rho \|\nabla_y (I \circ \tau - X)\|_1) \\ & + \lambda_2 \mu \sum_i \|\hat{P}_i \text{Vec}(X) - A_i\|_F^2 + \frac{\alpha}{2} \|I \circ \tau - X - R - \frac{J}{\alpha}\|_F^2. \end{aligned} \quad (5)$$

Due to the non-differentiability of the L_1 norm in (5), we apply the ADMM [22] by introducing auxiliary variables so as to split the original complex problem into several easy sub-problems with closed-form solutions. Thus, the L_1 -related subproblem can be solved via the soft shrinkage operator [22], and the L_2 -related subproblem can be computed in Fourier domain. The difference operator can be handled in fast Fourier transform (FFT) efficiently. The details can be found in the supplementary material.

It is worth noting, in our implementation, we replace the $\|\nabla_y (I \circ \tau - X)\|_1$ with $\|\nabla_y (X_t - X)\|_1$ where X_t is the intermediate result formed by the transformed image denoising result [Equation (4)]. The main reason is that the random noise free image follow our vertical gradient preserving observation more precisely. This also gives a physical meaning expression that the random noise and line pattern noise removal results are mutually reinforcing.

4) Update for $\Delta \tau$: Image transformation. The transformation can be obtained by solving following subproblem:

$$\Delta \hat{\tau} = \arg \min_{\Delta \tau} \|I \circ \tau + \nabla I \Delta \tau - X - R - \frac{J}{\alpha}\|_F^2. \quad (6)$$

The closed-form solution of (6) involves with computing the Moore-Penrose pseudoinverse of ∇I . And the initial-

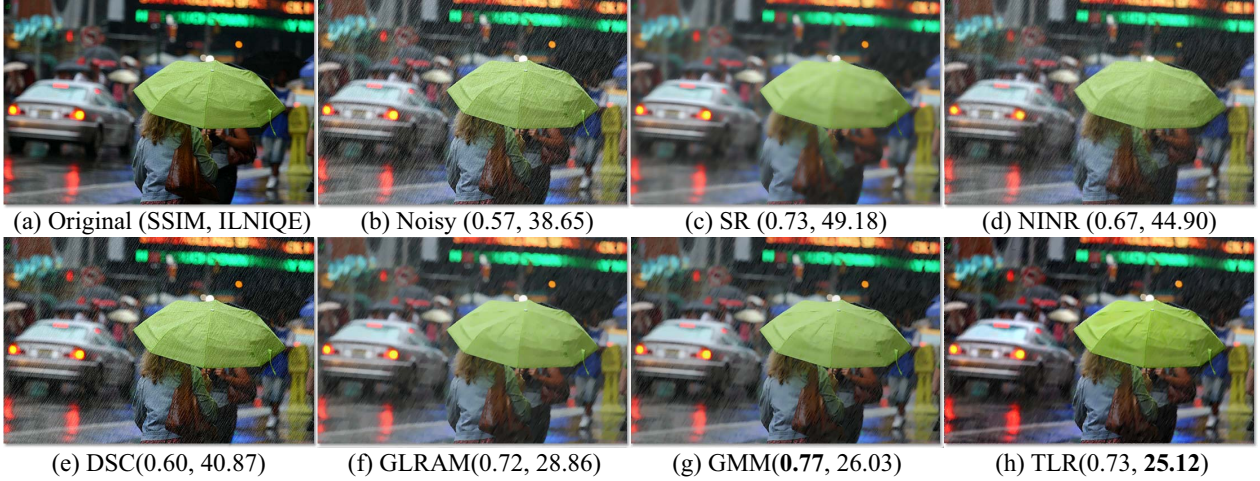


Figure 5. Simulated rain streak removal results of the dataset [19]. The rain streak here is light but dense.

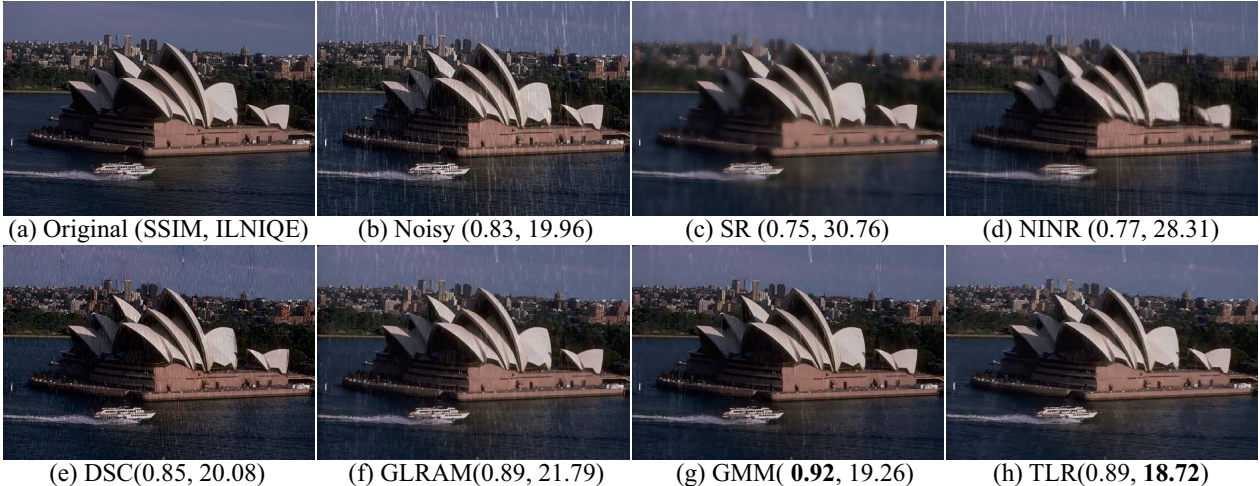


Figure 6. Simulated rain streak removal results of the dataset [21]. The rain streak here is sparse but bright.

ization of τ can be obtained by the TILT [36] in line pattern noise region with smoothing background. Thus, we have $\tau^{k+1} = \tau^k + \Delta\tau$. The algorithm procedure can be found in the supplementary material.

4. Experimental results

4.1. Experimental setting

The line pattern noise is ubiquitous in the real world. In this work, we choose two representative applications: rain streak and hyperspectral image stripe noise removal task to validate the effectiveness of our method. The configuration of the platform is on MATLAB 2014a, Intel i7 CPU at 3.6 GHz, and 32-GB memory. The Matlab code of proposed method can be downloaded at the author's homepage².

²<http://www.escience.cn/people/changyi/index.html>

4.2. Rain streak removal

Compared methods The state-of-the-art single image rain streak removal methods are selected for a full comparison, including the dictionary learning based SR [19], DSC[23], GLRAM [8], NINR [30], and the GMM [21]. All the parameters are fine-tuned by default or following the rules in their papers to achieve the best performance. Due to the space limitation, more results including the comparison with CNN [13] are included in the supplementary material.

Dataset and evaluation We evaluate the competing methods on three representative single image rain streak datasets [19, 23, 21], in which different kinds of rain streak appearance are considered. Both the full-reference assessment SSIM [31] (larger is better) and no-reference assessment IL-NIQE [35] (smaller is better) are employed to give an overall evaluation. We believe the no-reference assessment is



Figure 7. Real rain streak removal results of the dataset [23].

more appropriate, since it is closely associated with human subjective scores and features for subsequent application.

Results comparison Figure 5 and 6 show the simulated rain streak removal results, and Fig. 7 presents the real rain streak removal result. Note that the rain streak from different datasets have different appearance. We have the following observations. First, the proposed method achieves the best results with respect to both the visual appearance and the blind assessment ILNIQE. Second, The robustness of our method for different rain streak is superior to the competing methods. Our method obtains a better balance between rain streak removal and background texture preserving in all cases, while some other methods oversmooth the image background heavily [19, 31] or have obvious residual rain streak in the image background [23, 31, 8]. Third, compared with the most recent and competitive method [21], our result also shows slightly better rain streak removal (Fig. 5 and 6) and detail preserving (Fig. 7) performance. This demonstrates explicit utilization of directional property via both transformed low-rank and directional total variational plays a key role in line pattern modeling.

4.3. Hyperspectral stripe removal

Compared methods In hyperspectral image, the stripe always coexists with the random noise. However there is few single image base hyperspectral mixed noise removal method. We compare our method with the state-of-the-art multiple bands based hyperspectral image restoration methods, including 2-D low-rank methods LRMR [34], LRTV [16], MoG [27] and tensor-based methods BM4D [24], TDL [29], ISTReg [32], ASSTV (only vertical stripe) [5].

Dataset and evaluation The original size of Pavia University dataset³ is 610*340*103. Here, we select an 300*300*40 clean subcubic for simulation. Each band is degraded with the same level random and stripe noise.

The conventional PSNR and SSIM assessments are employed. For the real hyperspectral image, the size of dataset CHRIS_FY⁴ is 766*748*18. We select an 590*590*18 subcubic without the black boundary for test.

Results comparison Figure 8 and 9 show the simulated and real stripe removal results, respectively. We have the following observations. First, most of the previous methods are effective for the random noise, but fail to remove stripes satisfactorily. On the contrary, our method is capable of handling the real complex noise scenarios. Second, our single image based method is even superior to the state-of-the-art multiple based hyperspectral image restoration methods, both in terms of quantitative assessments and qualitative visual appearance. This strongly demonstrates that the importance of the reasonable modeling for the image layers in spatial domain, while previous methods pay much attention to the spectral correlation. Our work may provide a new perspective for hyperspectral image mixed noise removal.

4.4. Limitation

The rotation operator and directional property are both double-edged sword for the line pattern modeling. Once the rotation operator is called, the high-frequency information reduction caused by the interpolation will be unavoidable. This is an inherent flaw of our method. For the directional property, it not only facilitates to remove the line pattern noise, but also takes away the image structure with the same direction as the line pattern noise unexpectedly (As shown in Fig. 3, the estimated rain streak layer contains the texture with same direction as rain streak, though the other texture have been affected a little). This problem is deeply rooted in all single image decomposition based line pattern noise removal methods, since it is hard to completely distinguish the line pattern noise and the similar image edges in an unsupervised manner or without any additional informa-

³http://www.ehu.eus/ccwintco/index.php?title=Hyperspectral_Remote_Sensing_Scenes

⁴<http://www.brockmann-consult.de/beam/data/products/>

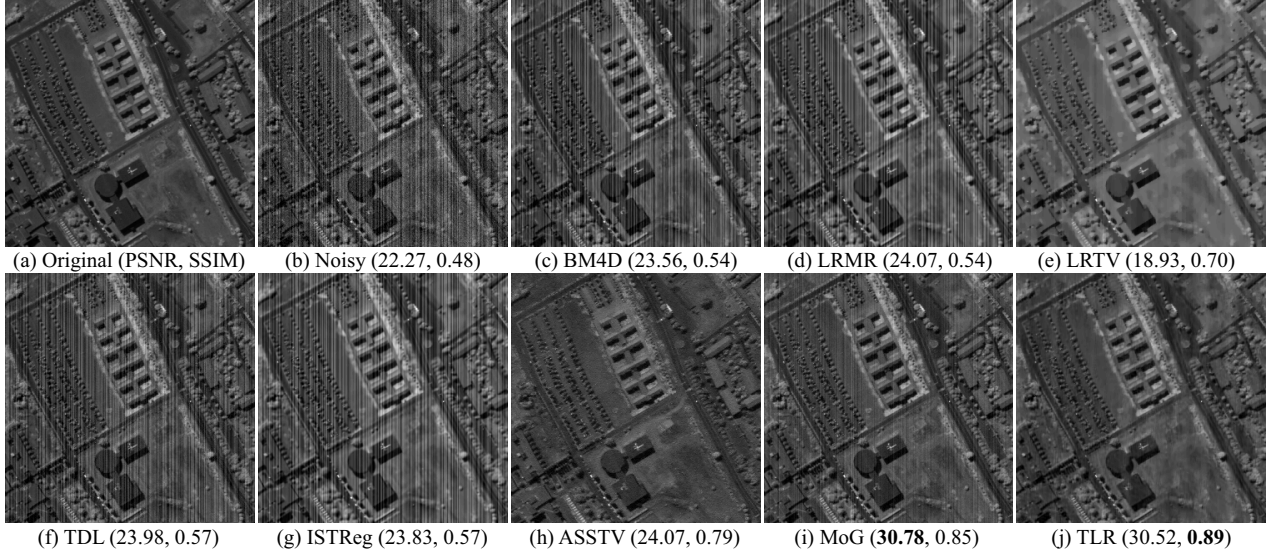


Figure 8. Simulated mixed random and stripe noise removal results of hyperspectral dataset. Note that all the competing methods need multiple image bands, while our method is single image based.

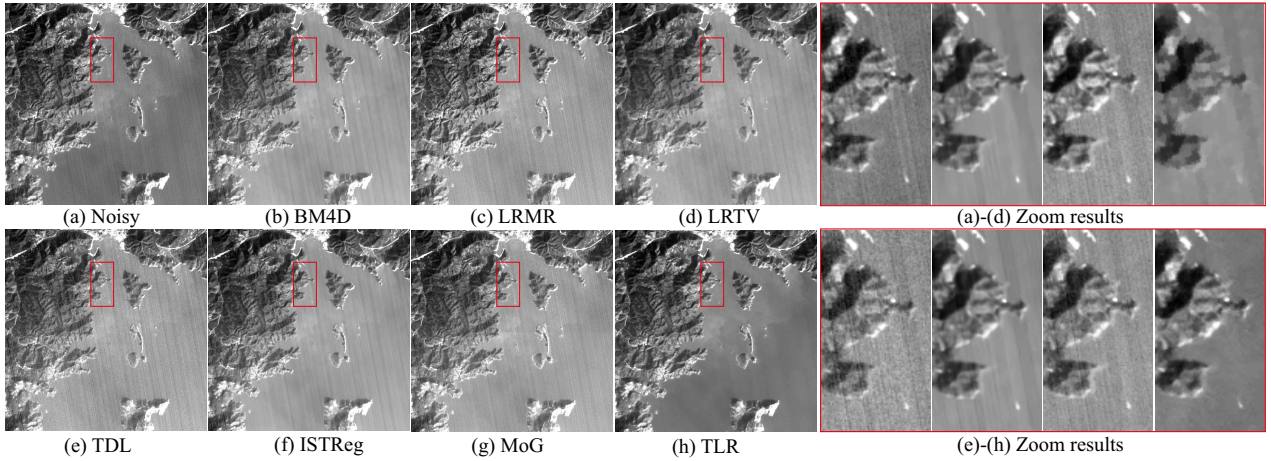


Figure 9. Real mixed random and stripe noise removal results of the hyperspectral dataset.

tion. To remedy this, incorporating the additional spectral or temporal information to the decomposition-based framework or learning the rain streak specific based CNN may facilitate to advance this issue.

5. Conclusion

In this work, we propose a novel transformed low-rank image decomposition framework for line pattern noise removal. We explicitly utilize the directional property of the line pattern in the transformed domain, where the subspace is more compact than that of the original image domain. This contributes to better separation between the line pattern layer and image layer. Moreover, we analyze the detailed discrepancy between the mixed noise degraded im-

age and clean image, in which both the local directional gradient and nonlocal self-similarity information has been involved. With present prevalent of spectral or temporal correlation modeling, we offer an new perspective from the spatial transformed domain. Compared to the recent single image based methods, this compositional prior suggests that better modeling for the image layer may have more impact on mixed random and line pattern noise issue. The proposed method has been tested on rain streak and hyperspectral stripe removal, and it consistently achieves state-of-the-art performance.

Acknowledgements. This work was supported by the projects of the National Natural Science Foundation of China under Grant 61571207 and Grant 61433007.

References

- [1] A. Buades, B. Coll, and J. M. Morel. A non-local algorithm for image denoising. In *CVPR*, pages 60–65, 2005.
- [2] H. C. Burger, C. J. Schuler, and S. Harmeling. Image denoising: Can plain neural networks compete with bm3d? In *CVPR*, pages 2392–2399, 2012.
- [3] J.-F. Cai, E. J. Candès, and Z. Shen. A singular value thresholding algorithm for matrix completion. *SIAM J. on Optim.*, 20(4):1956–1982, 2010.
- [4] X. Cao, Y. Chen, Q. Zhao, D. Meng, Y. Wang, D. Wang, and Z. Xu. Low-rank matrix factorization under general mixture noise distributions. In *ICCV*, pages 1493–1501, 2015.
- [5] Y. Chang, L. Yan, H. Fang, and C. Luo. Anisotropic spectral-spatial total variation model for multispectral remote sensing image destriping. *IEEE TIP*, 24(6):1852–1866, 2015.
- [6] Y. Chang, L. Yan, T. Wu, and S. Zhong. Remote sensing image stripe noise removal: From image decomposition perspective. *IEEE TGRS*, 54(12):7018–7031, 2016.
- [7] Y. Chang, L. Yan, and S. Zhong. Hyper-laplacian regularized unidirectional low-rank tensor recovery for multispectral image denoising. In *CVPR*, pages 4260–4268, 2017.
- [8] Y. L. Chen and C. T. Hsu. A generalized low-rank appearance model for spatio-temporally correlated rain streaks. In *ICCV*, pages 1968–1975, 2013.
- [9] W. Dong, G. Li, G. Shi, X. Li, and Y. Ma. Low-rank tensor approximation with laplacian scale mixture modeling for multiframe image denoising. In *ICCV*, pages 442–449, 2015.
- [10] W. Dong, X. Li, L. Zhang, and G. Shi. Sparsity-based image denoising via dictionary learning and structural clustering. In *CVPR*, pages 457–464, 2011.
- [11] J. Fehrenbach, P. Weiss, and C. Lorenzo. Variational algorithms to remove stationary noise: applications to microscopy imaging. *IEEE TIP*, 21(10):4420–30, 2012.
- [12] C. Fernandez-granda and E. J. Candes. Super-resolution via transform-invariant group-sparse regularization. In *ICCV*, pages 3336–3343, 2013.
- [13] X. Fu, J. Huang, X. Ding, Y. Liao, and J. Paisley. Clearing the skies: A deep network architecture for single-image rain removal. *IEEE TIP*, 26(6):2944–2956, 2017.
- [14] K. Garg and S. K. Nayar. Vision and rain. *IJCV*, 75(1):3–27, 2007.
- [15] S. Gu, L. Zhang, W. Zuo, and X. Feng. Weighted nuclear norm minimization with application to image denoising. In *CVPR*, pages 2862–2869, 2014.
- [16] W. He, H. Zhang, L. Zhang, and H. Shen. Total-variation-regularized low-rank matrix factorization for hyperspectral image restoration. *IEEE TGRS*, 54(1):178–188, 2016.
- [17] K. H. Jensen, F. Sigworth, and S. S. Brandt. Removal of vesicle structures from transmission electron microscope images. *IEEE TIP*, 25(2):540–552, 2016.
- [18] H. S. Jung, J. S. Won, M. H. Kang, and Y. W. Lee. Detection and restoration of defective lines in the spot 4 swir band. *IEEE TIP*, 19(8):2143–56, 2010.
- [19] L. W. Kang, C. W. Lin, and Y. H. Fu. Automatic single-image-based rain streaks removal via image decomposition. *IEEE TIP*, 21(4):1742–1755, 2012.
- [20] J. H. Kim, C. Lee, J. Y. Sim, and C. S. Kim. Single-image deraining using an adaptive nonlocal means filter. In *ICIP*, pages 914–917, 2013.
- [21] Y. Li, T. R. Tan, X. Guo, J. Lu, and B. S. Michael. Rain streak removal using layer priors. In *CVPR*, pages 2736–2744, 2016.
- [22] Z. Lin, R. Liu, and Z. Su. Linearized alternating direction method with adaptive penalty for low-rank representation. In *NIPS*, pages 612–620, 2011.
- [23] Y. Luo, Y. Xu, and H. Ji. Removing rain from a single image via discriminative sparse coding. In *ICCV*, pages 3397–3405, 2015.
- [24] M. Maggioni, V. Katkovnik, K. Egiazarian, and A. Foi. Nonlocal transform-domain filter for volumetric data denoising and reconstruction. *IEEE TIP*, 22(1):119–33, 2012.
- [25] M. Maggioni, E. Snchez-Monge, and A. Foi. Joint removal of random and fixed-pattern noise through spatiotemporal video filtering. *IEEE TIP*, 23(10):4282–4296, 2014.
- [26] J. Mairal, F. Bach, J. Ponce, G. Sapiro, and A. Zisserman. Non-local sparse models for image restoration. In *ICCV*, pages 2272–2279, 2009.
- [27] D. Meng and F. D. L. Torre. Robust matrix factorization with unknown noise. In *ICCV*, pages 1337–1344, 2013.
- [28] Y. Peng, A. Ganesh, J. Wright, and W. Xu. Rasl: Robust alignment by sparse and low-rank decomposition for linearly correlated images. In *CVPR*, pages 763–770, 2010.
- [29] Y. Peng, D. Meng, Z. Xu, C. Gao, Y. Yang, and B. Zhang. Decomposable nonlocal tensor dictionary learning for multispectral image denoising. In *CVPR*, pages 2949–2956, 2014.
- [30] R. Wang and E. Trucco. Single-patch low-rank prior for non-pointwise impulse noise removal. In *ICCV*, pages 1073–1080, 2013.
- [31] Z. Wang, A. C. Bovik, H. R. Sheikh, and E. P. Simoncelli. Image quality assessment: from error visibility to structural similarity. *IEEE TIP*, 13(4):600–612, 2004.
- [32] Q. Xie, Q. Zhao, D. Meng, Z. Xu, S. Gu, W. Zuo, and L. Zhang. Multispectral images denoising by intrinsic tensor sparsity regularization. In *CVPR*, pages 1692–1700, 2016.
- [33] J. Xu, L. Zhang, W. Zuo, D. Zhang, and X. Feng. Patch group based nonlocal self-similarity prior learning for image denoising. In *ICCV*, pages 244–252, 2015.
- [34] H. Zhang, W. He, L. Zhang, H. Shen, and Q. Yuan. Hyperspectral image restoration using low-rank matrix recovery. *IEEE TGRS*, 52(8):4729–4743, 2014.
- [35] L. Zhang, L. Zhang, and A. C. Bovik. A feature-enriched completely blind image quality evaluator. *IEEE TIP*, 24(8):2579–91, 2015.
- [36] Z. Zhang, A. Ganesh, X. Liang, and Y. Ma. Tilt: Transform invariant low-rank textures. *IJCV*, 99(1):1–24, 2012.
- [37] Q. Zhao, D. Meng, X. Kong, Q. Xie, W. Cao, Y. Wang, and Z. Xu. A novel sparsity measure for tensor recovery. In *ICCV*, pages 271–279, 2015.
- [38] F. Zhu, G. Chen, and P. A. Heng. From noise modeling to blind image denoising. In *CVPR*, pages 420–429, 2016.
- [39] D. Zoran and Y. Weiss. From learning models of natural image patches to whole image restoration. In *ICCV*, pages 479–486, 2011.

Supplementary Material for “Transformed Low-rank Model for Line Pattern Noise Removal”

Yi Chang, Luxin Yan*, Sheng Zhong

National Key Laboratory of Science and Technology on Multispectral Information Processing
School of Automation, Huazhong University of Science and Technology, China

{yichang, yanluxin, zhongsheng}@hust.edu.cn

1. Solution to Problem (5) in Main Text

The original problem is shown as follow:

$$\hat{\mathbf{X}} = \arg \min_{\mathbf{X}} \lambda_1 (\|\nabla_x \mathbf{X}\|_1 + \rho \|\nabla_y (\mathbf{I} \circ \tau - \mathbf{X})\|_1) + \lambda_2 \mu \sum_i \|\hat{\mathbf{P}}_i \text{Vec}(\mathbf{X}) - \mathbf{A}_i\|_F^2 + \frac{\alpha}{2} \|\mathbf{I} \circ \tau + \nabla \mathbf{I} \Delta \tau - \mathbf{X} - \mathbf{R} - \frac{\mathbf{J}}{\alpha}\|_F^2. \quad (1)$$

The main difficulty for solving the problem (1) directly lies in the non-differentiability of the L_1 norm and the patch operation \mathbf{P}_i . Naturally, we introduce three auxiliary variables, by applying ADMM to (1). Thus we obtain

$$\begin{aligned} \{\hat{\mathbf{X}}, \hat{\mathbf{Z}}, \hat{\mathbf{D}}_x, \hat{\mathbf{D}}_y\} &= \arg \min_{\mathbf{X}, \mathbf{Z}, \mathbf{D}_x, \mathbf{D}_y} \lambda_2 \mu \sum_i \|\hat{\mathbf{P}}_i \mathbf{Z} - \mathbf{A}_i\|_F^2 + \frac{\eta}{2} \|\mathbf{Z} - \text{Vec}(\mathbf{X}) - \frac{\mathbf{J}_z}{\eta}\|_F^2 + \frac{\alpha}{2} \|\mathbf{I} \circ \tau + \nabla \mathbf{I} \Delta \tau - \mathbf{X} - \mathbf{R} - \frac{\mathbf{J}}{\alpha}\|_F^2 \\ &\quad + \lambda_1 \|\mathbf{D}_x\|_1 + \frac{\beta}{2} \|\mathbf{D}_x - \nabla_x \mathbf{X} - \frac{\mathbf{J}_x}{\beta}\|_F^2 + \lambda_1 \rho \|\mathbf{D}_y\|_1 + \frac{\gamma}{2} \|\mathbf{D}_y - \nabla_y (\mathbf{I} \circ \tau - \mathbf{X}) - \frac{\mathbf{J}_y}{\gamma}\|_F^2, \end{aligned} \quad (2)$$

where $\mathbf{Z}, \mathbf{D}_x, \mathbf{D}_y$ are the auxiliary variables, $\mathbf{J}_x, \mathbf{J}_y, \mathbf{J}_z$ are the corresponding Lagrangian multiplier, and β, γ, η are the positive scalars. The problem can be solved via alternating minimization:

$$\mathbf{X}^{k+1} = \arg \min_{\mathbf{X}} \frac{\alpha}{2} \|\mathbf{I} \circ \tau + \nabla \mathbf{I} \Delta \tau - \mathbf{X} - \mathbf{R} - \frac{\mathbf{J}}{\alpha}\|_F^2 + \frac{\beta}{2} \|\mathbf{D}_x^k - \nabla_x \mathbf{X} - \frac{\mathbf{J}_x^k}{\beta}\|_F^2 + \frac{\gamma}{2} \|\mathbf{D}_y^k - \nabla_y (\mathbf{I} \circ \tau - \mathbf{X}) - \frac{\mathbf{J}_y^k}{\gamma}\|_F^2 + \frac{\eta}{2} \|\mathbf{Z}^k - \text{Vec}(\mathbf{X}^k) - \frac{\mathbf{J}_z^k}{\eta}\|_F^2, \quad (3)$$

$$\mathbf{Z}^{k+1} = \arg \min_{\mathbf{Z}} \lambda_2 \mu \sum_i \|\hat{\mathbf{P}}_i \mathbf{Z} - \mathbf{A}_i\|_F^2 + \frac{\eta}{2} \|\mathbf{Z} - \text{Vec}(\mathbf{X}^{k+1}) - \frac{\mathbf{J}_z^{k+1}}{\eta}\|_F^2, \quad (4)$$

$$\mathbf{D}_x^{k+1} = \arg \min_{\mathbf{D}_x} \lambda_1 \|\mathbf{D}_x\|_1 + \frac{\beta}{2} \|\mathbf{D}_x - \nabla_x \mathbf{X}^{k+1} - \frac{\mathbf{J}_x^k}{\beta}\|_F^2, \quad (5)$$

$$\mathbf{D}_y^{k+1} = \arg \min_{\mathbf{D}_y} \lambda_1 \rho \|\mathbf{D}_y\|_1 + \frac{\gamma}{2} \|\mathbf{D}_y - \nabla_y (\mathbf{I} \circ \tau - \mathbf{X}^{k+1}) - \frac{\mathbf{J}_y^k}{\gamma}\|_F^2. \quad (6)$$

Consequently, subproblem (3) has the closed-formed solution and can be computed in the fast Fourier transform domain due to the differential operator, subproblem (4) can be computed in pixel-to-pixel level division, which can be regarded as the aggregation operation in these overlapped regions due to the \mathbf{P}_i , and the subproblem (5) and (6) is solved via the soft shrinkage operator efficiently. The Lagrangian multiplier and positive scalars can be updated as follows:

$$\begin{cases} \mathbf{J}_z^{k+1} = \mathbf{J}_z^k + \eta^k (\text{Vec}(\mathbf{X}^{k+1}) - \mathbf{Z}^{k+1}) \\ \mathbf{J}_x^{k+1} = \mathbf{J}_x^k + \beta^k (\nabla_x \mathbf{X}^{k+1} - \mathbf{D}_x^{k+1}) \\ \mathbf{J}_y^{k+1} = \mathbf{J}_y^k + \gamma^k (\nabla_y (\mathbf{I} \circ \tau - \mathbf{X}^{k+1}) - \mathbf{D}_y^{k+1}). \end{cases} \quad (7)$$

$$\begin{cases} \eta^{k+1} = \kappa \eta^k \\ \beta^{k+1} = \kappa \beta^k \\ \gamma^{k+1} = \kappa \gamma^k. \end{cases} \quad (8)$$

When applying ADMM, the problem with less than three alternating terms usually converges. There are four variables to be estimated, and the convergence of problem (1) via ADMM can not be guaranteed. However, since each subproblem has the closed-formed solution, with proper parameter setting and initialization, we empirically find the proposed method can always obtain a satisfactory result. The running time for an image with size 481×321 is about 7 minutes with unoptimized Matlab code. The algorithm procedure of problem (1) is summarized in **Algorithm 1**. And the whole algorithm in the main text is shown in **Algorithm 2**¹. Our algorithm includes both the outside loop and inner loop, which is very common in image processing.

Algorithm 1 The innerloop for solving problem (1), namely the problem (5) in main text

Require: The transformed image $\mathbf{I} \circ \tau$, line pattern component \mathbf{R}, \mathbf{J}

- 1: **Initialize:**
- 2: • Set parameters $\lambda_1, \lambda_2, \rho, \mu, \alpha, \beta, \gamma, \eta, \kappa$;
- 3: • Set $\mathbf{J}_x^{(1)} = 0, \mathbf{J}_y^{(1)} = 0, \mathbf{J}_z^{(1)} = 0$;
- 4: **for** $k=1:K$ **do**
- 5: Obtain $\mathbf{X}^{(k+1)}$ via solving Eq. (3);
- 6: Compute $\mathbf{Z}^{(k+1)}$ via solving Eq. (4);
- 7: Solve Eq. (5) for $\mathbf{D}_x^{(k+1)}$;
- 8: Solve Eq. (6) for $\mathbf{D}_y^{(k+1)}$;
- 9: Update $\mathbf{J}_x^{(k+1)}, \mathbf{J}_y^{(k+1)}, \mathbf{J}_z^{(k+1)}$ via Eq. (7);
- 10: Update $\eta^{(k+1)}, \beta^{(k+1)}, \gamma^{(k+1)}$ via Eq. (8);
- 11: Output the clear image \mathbf{X} if $k = K$.
- 12: **end for**

Ensure: Solution \mathbf{X} to problem (1).

Algorithm 2 The transformed low-rank (TLR) algorithm

Require: Input image \mathbf{I}

- 1: **Initialize:**
- 2: • initial affine transformation τ ;
- 3: • Set parameters as in Algorithm 1;
- 4: **for** $n=1:N$ **do**
- 5: **Line pattern noise estimation:** obtain \mathbf{B} by solving Eq. (3);
- 6: **Random noise removal:** solve Eq. (4) for \mathbf{A}_i ;
- 7: **Image restoration:** compute \mathbf{X} via Eq. (5) (Algorithm 1);
- 8: **Image transformation:** update $\Delta\tau$ via Eq. (6);
- 9: Output the clear image \mathbf{X} if $n = N$.
- 10: **end for**

Ensure: Clean Image \mathbf{X} .

2. More results

In this document, we present more results, which are not included in the main paper due to page limit.

2.1. Rain Streak Removal Results

Figure 1 to Figure 3 present three visual rain streak removal results on dataset [2] including the CNN based method [1]. Figure 4 to Figure 6 show three visual rain streak removal results on dataset [3]. Figure 7 and 8 show two real rain streak image removal results on dataset [4]. The proposed TLR method show obvious advantage over the state-of-the-art methods in terms of both rain streak removal and image structure preserving under various kinds of rain streak. For example, in Fig. 6 with severe rain streak, while previous methods over-smooth the image content unexpectedly (see the cloud marked by the ellipse), our method preserves the details much better. On the other hand, in Fig. 8, we can observe that our method removes the rain streak completely, while the competing methods fail to handle this situation (see from the zoom regions).

¹Note that, the equations in Algorithm 2 refer to the main text.

2.2. Hyperspectral Stripe Removal Results

In this section, we present the comparison results on hyperspectral image dataset *Urban*². The size of this dataset is 307*307*210. We present the visual stripe removal results and also the corresponding mean cross-track profiles (the horizontal axis represents the row/column number across the stripe, and the vertical axis means the corresponding digital number value of each row/column). Here, we choose three sub-bands: band 1, band 103 and band 152 as representative. In Fig. 9, Fig. 11 and Fig. 13, it can be observed that the images restored by our method are more visually pleasant with more detailed information and noise-free performance. The corresponding mean cross-track profiles as shown in Fig. 10, Fig. 12 and Fig. 14 further validate the effectiveness of our method for stripe removal, since the curves of our method are much more smoother than that of the others.

2.3. Large scale data low-rank property analysis

In this section, we verify the low-rank property for both the image and rain streak patch on large scale data. First, we collect 149625 non-local similar image patch with the size 36 * 100, and 124644 rotated rain patches with the size 40 * 40. In Fig. 15(a) and (b), we perform the SVD on the collected patches for both the image and rain, respectively. We can observe that the rain streak with the line pattern appearance has an extremely distinct low rank structure, while the constructed similar image patches also possess a relative higher low-rank property. Thus, it is reasonable for us to enforce the low-rank constraint on both the image and line pattern patch layer.

²<http://www.tec.army.mil/hypercube>

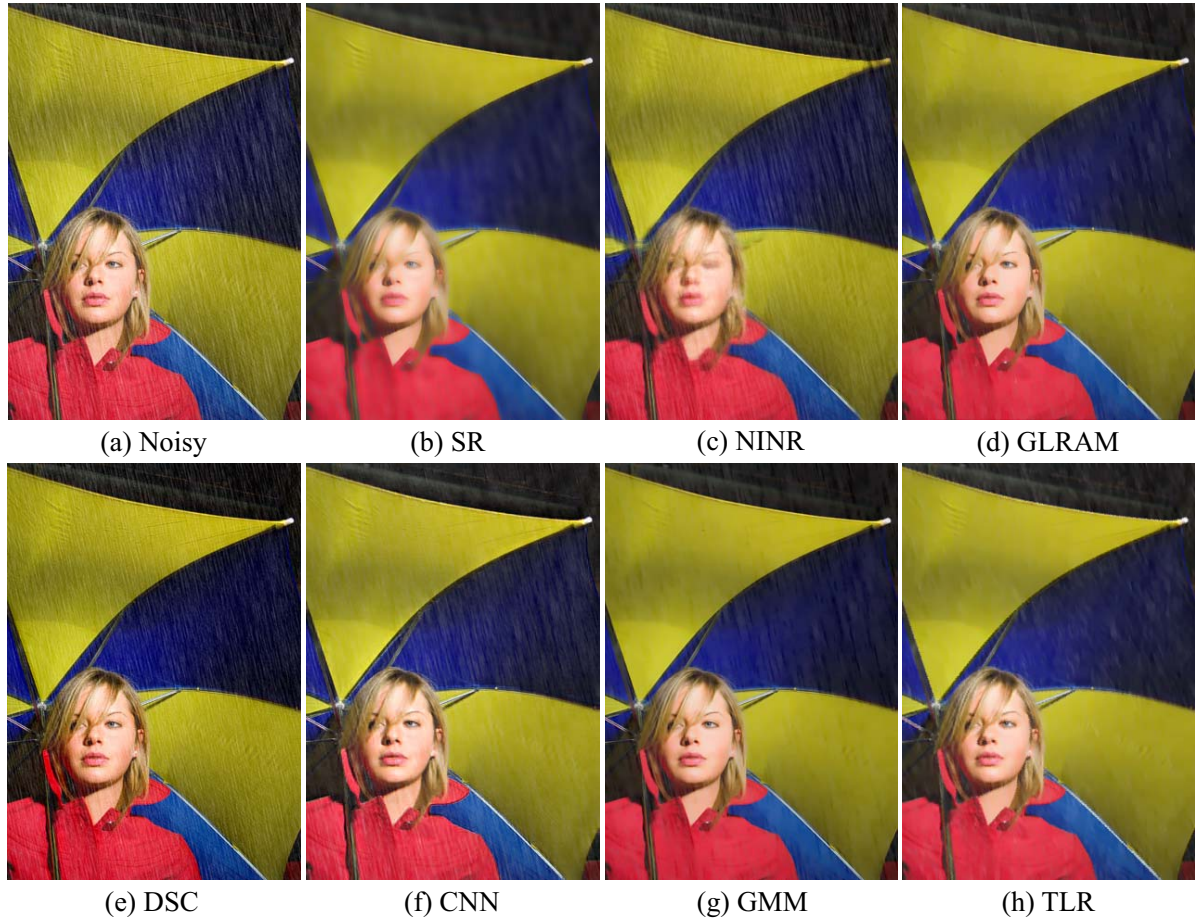


Figure 1. Rain streak removal results of image *Umbrella* on dataset [2].



(a) Rain image



(b) SR



(c) NINR



(d) GLRAM



(e) DSC



(f) CNN



(g) GMM



(h) TLR

Figure 2. Rain streak removal results of image *Cat and Dog* on dataset [2].

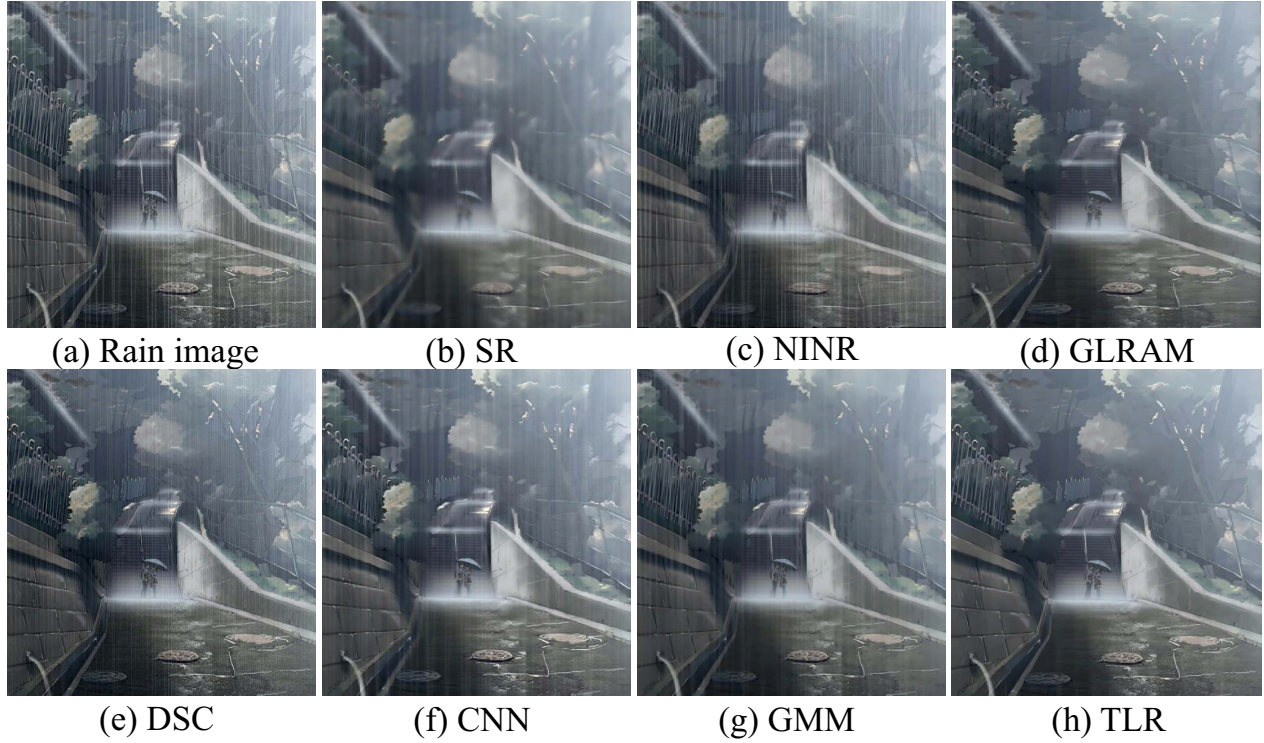


Figure 3. Rain streak removal results of image *Couples* on dataset [2].

References

- [1] X. Fu, J. Huang, X. Ding, Y. Liao, and J. Paisley. Clearing the skies: A deep network architecture for single-image rain removal. *IEEE TIP*, 26(6):2944–2956, 2017.
- [2] L. W. Kang, C. W. Lin, and Y. H. Fu. Automatic single-image-based rain streaks removal via image decomposition. *IEEE TIP*, 21(4):1742–1755, 2012.
- [3] Y. Li, T. R. Tan, X. Guo, J. Lu, and B. S. Michael. Rain streak removal using layer priors. In *CVPR*, pages 2736–2744, 2016.
- [4] Y. Luo, Y. Xu, and H. Ji. Removing rain from a single image via discriminative sparse coding. In *ICCV*, pages 3397–3405, 2015.

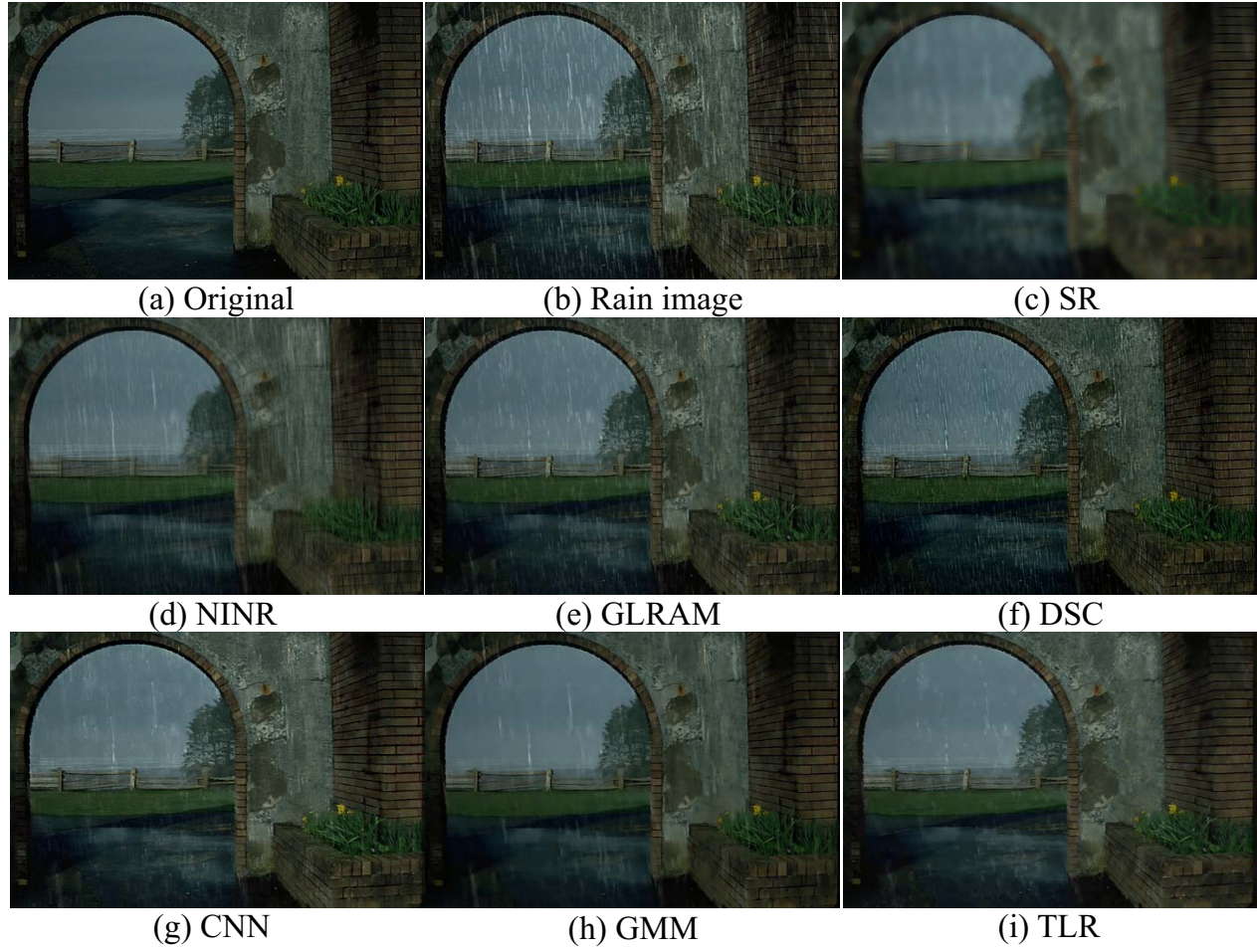


Figure 4. Rain streak removal results of image *Arch door* on dataset [3].

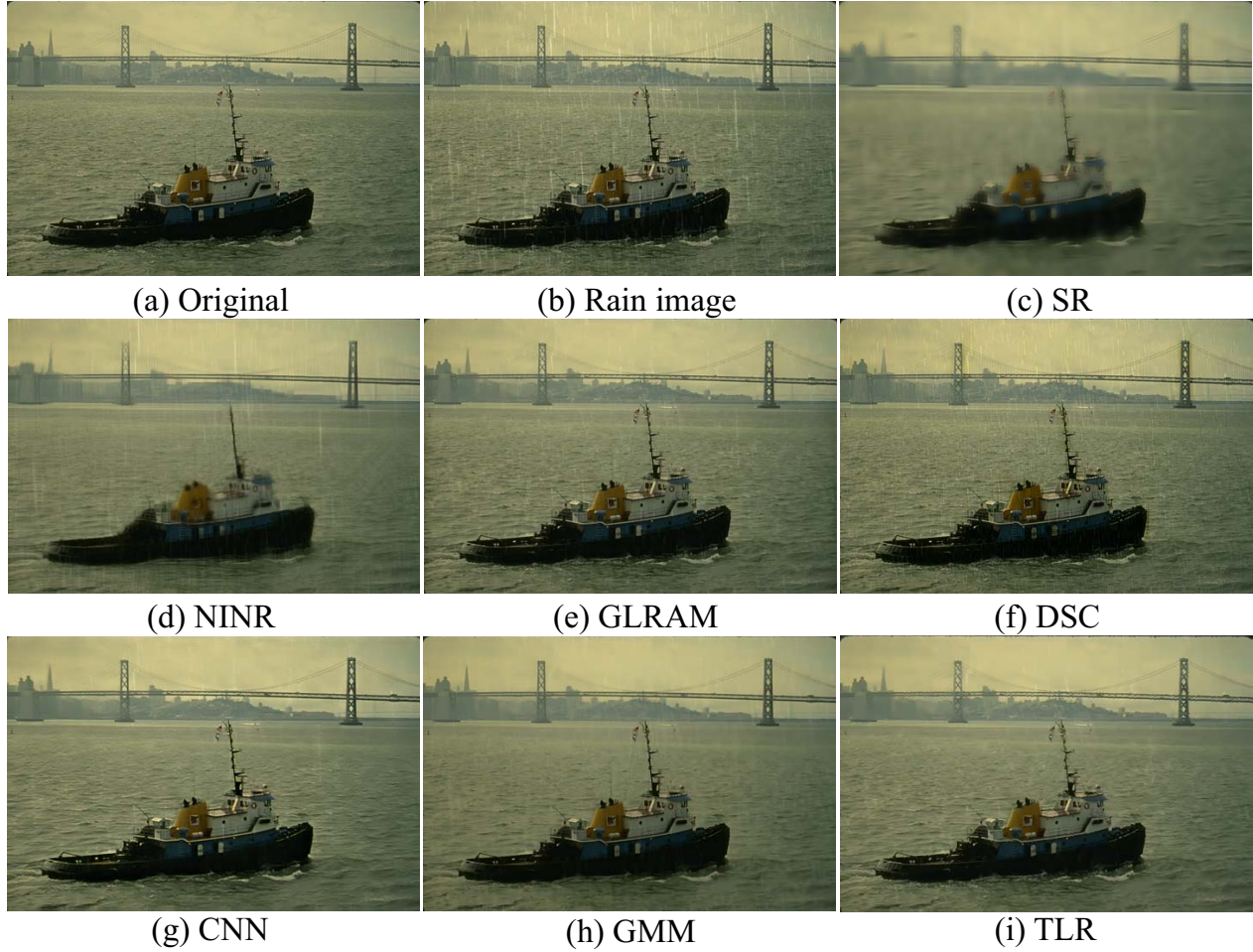


Figure 5. Rain streak removal results of image *Ship* on dataset [3].

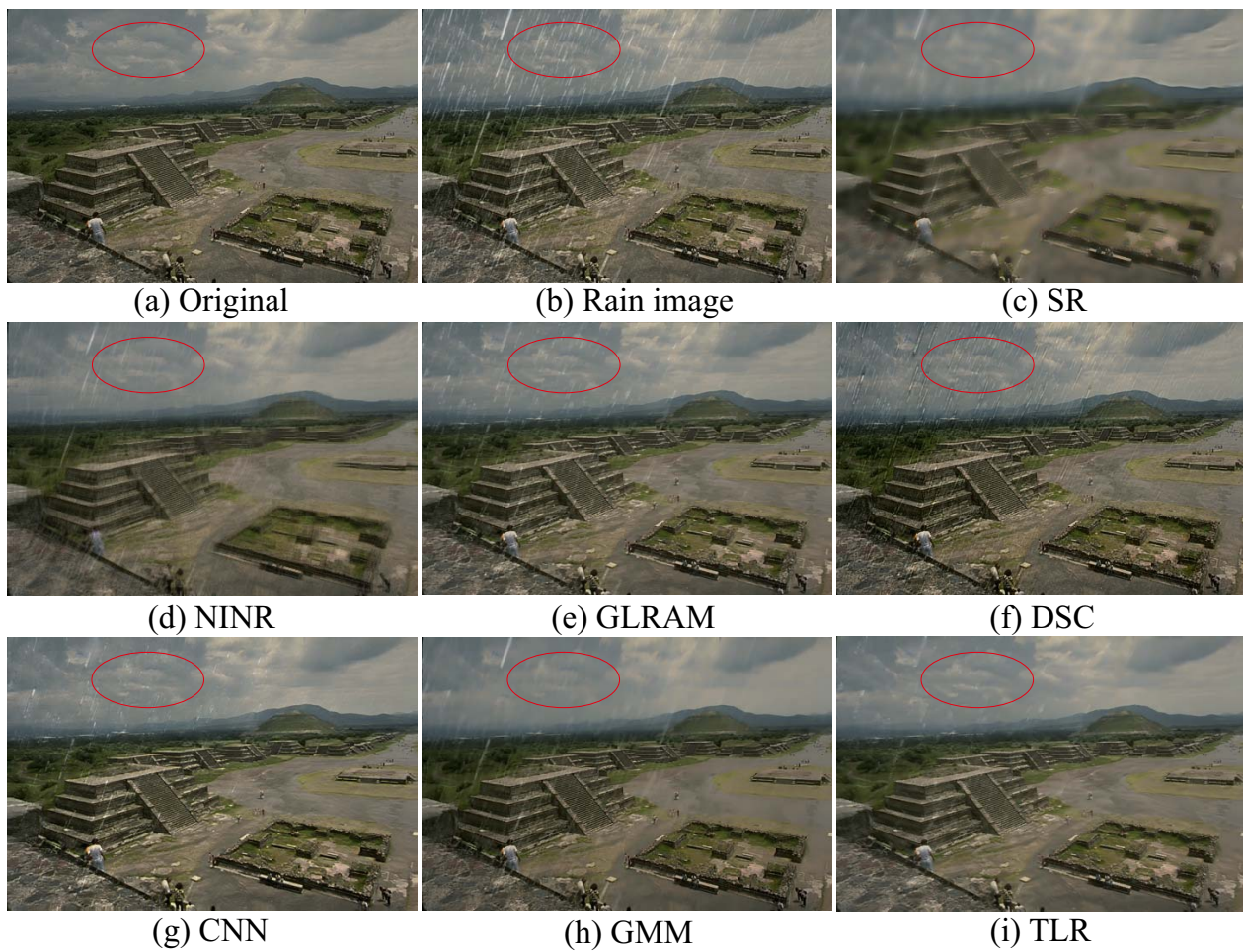


Figure 6. Rain streak removal results of image *Scenery* on dataset [3].

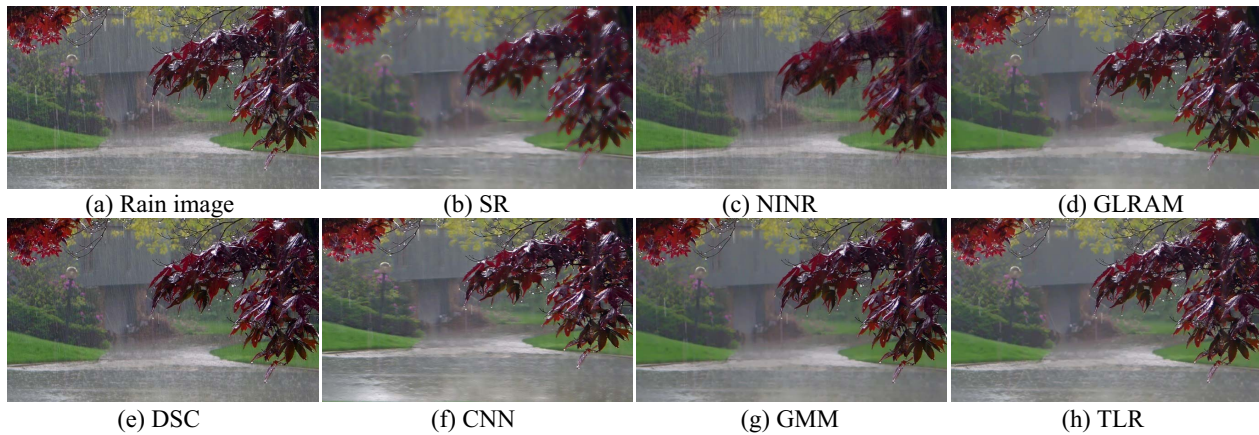


Figure 7. Rain streak removal results of image *Street* on dataset [4].

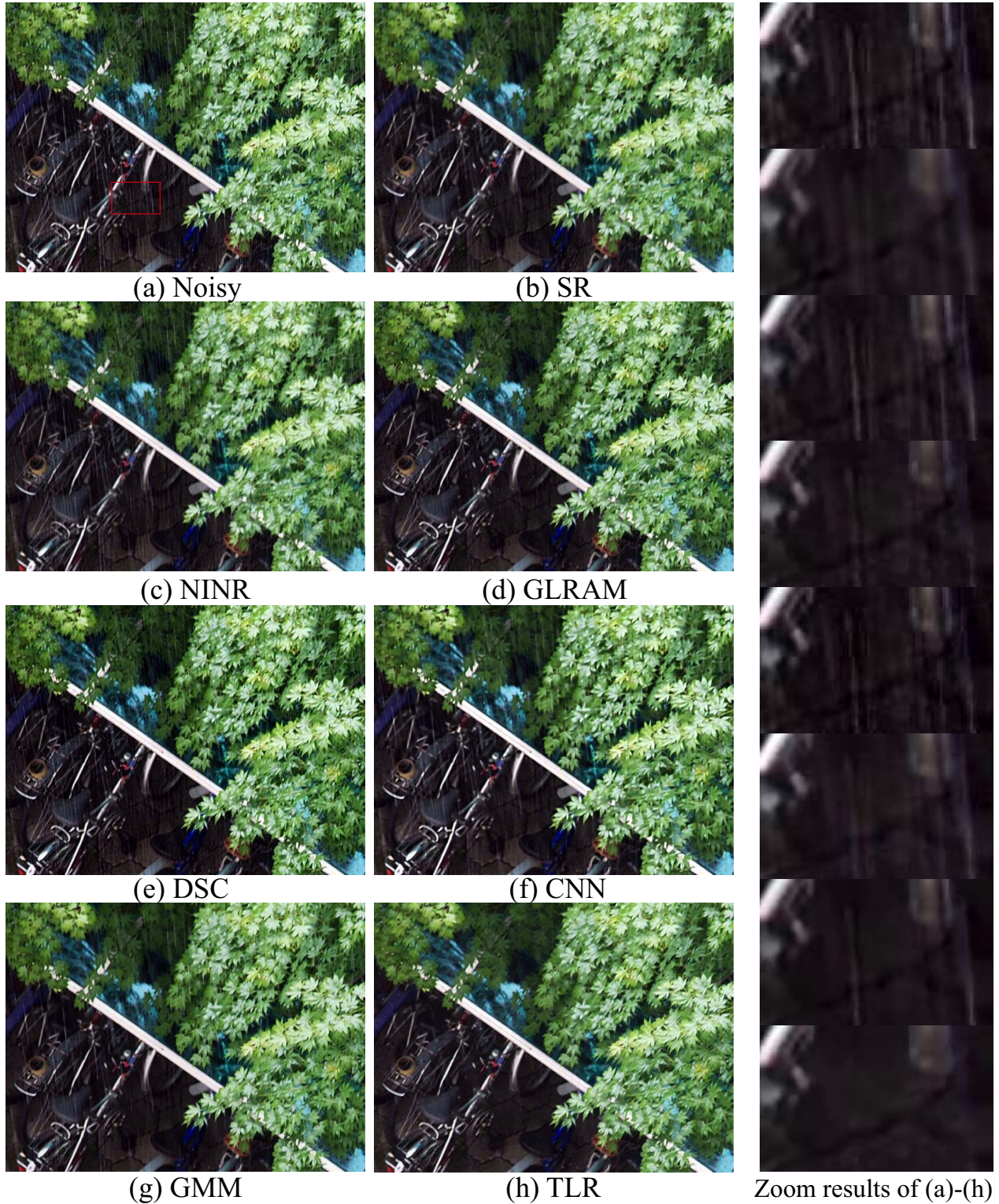


Figure 8. Rain streak removal results of image *Bicycle* on dataset [4].

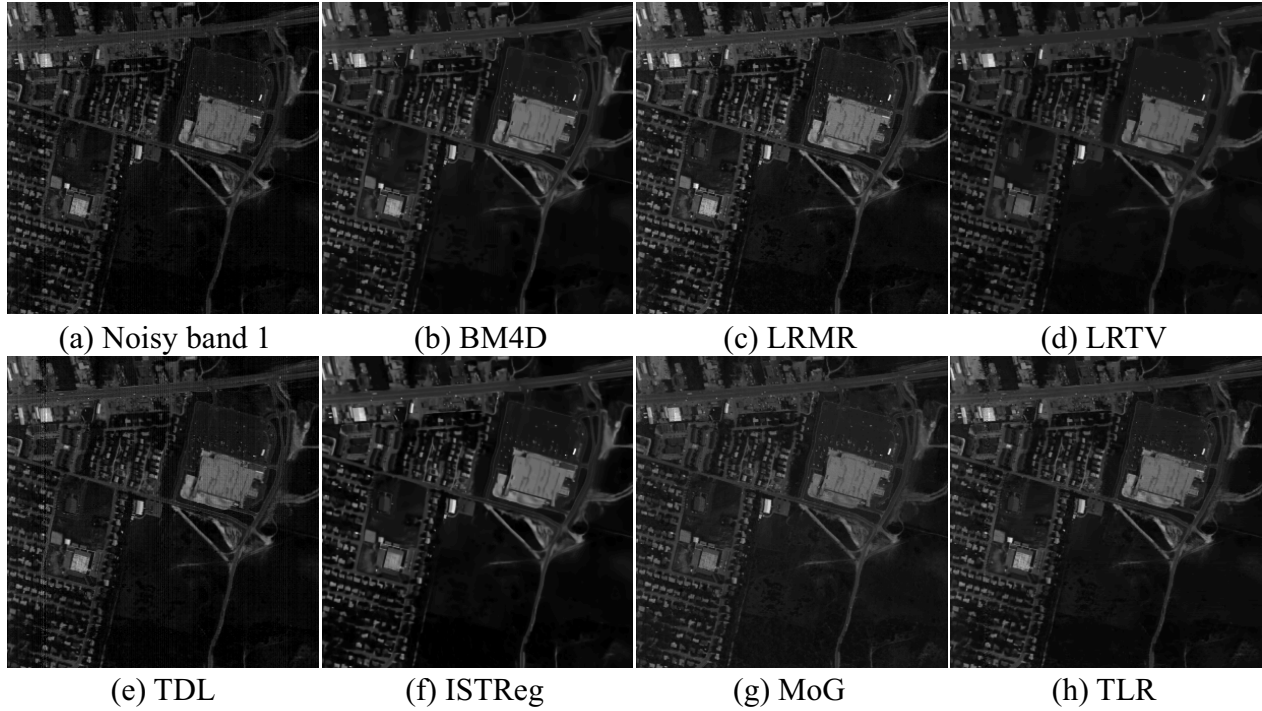


Figure 9. Hypersepctral image *Urban* stripe noise removal results of band 1.

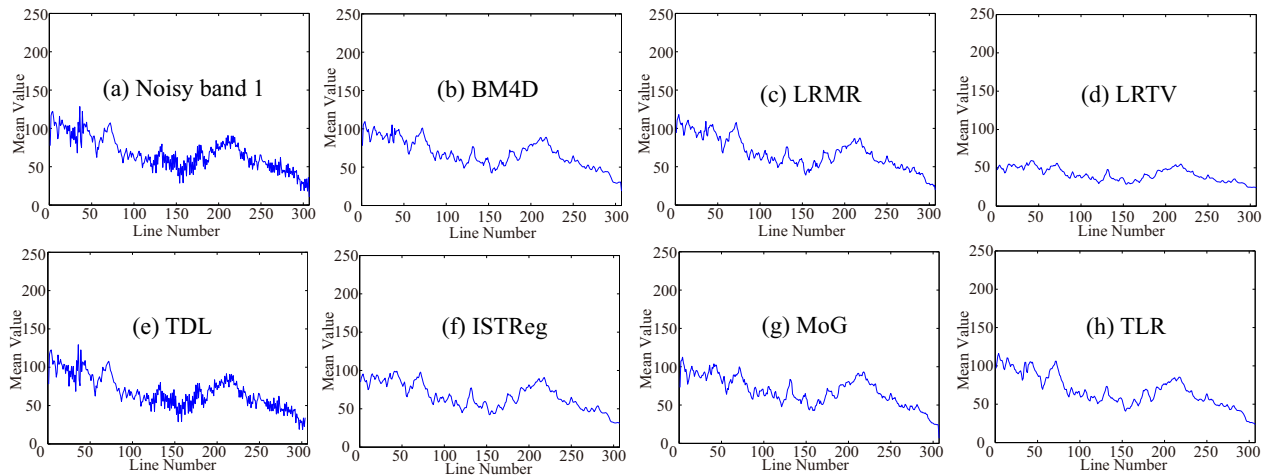


Figure 10. Mean cross-track profiles for images shown in Fig. 9.

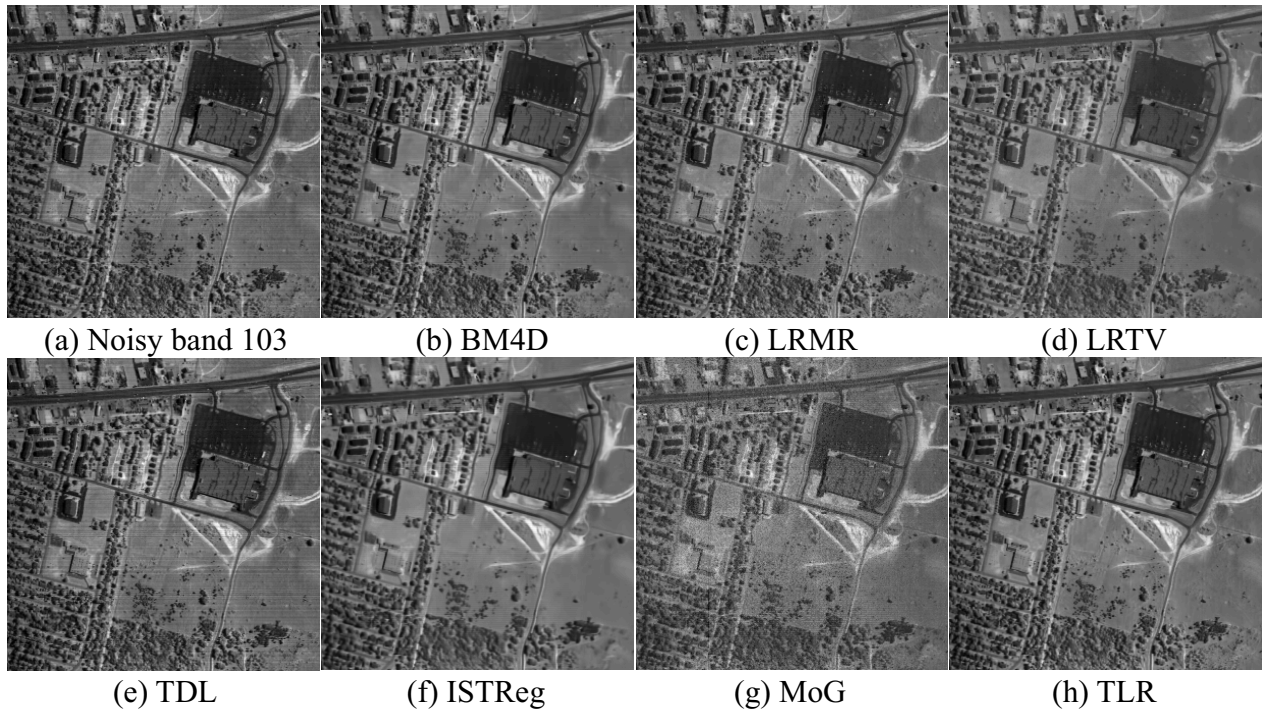


Figure 11. Hypersepctral image *Urban* stripe noise removal results of band 103.

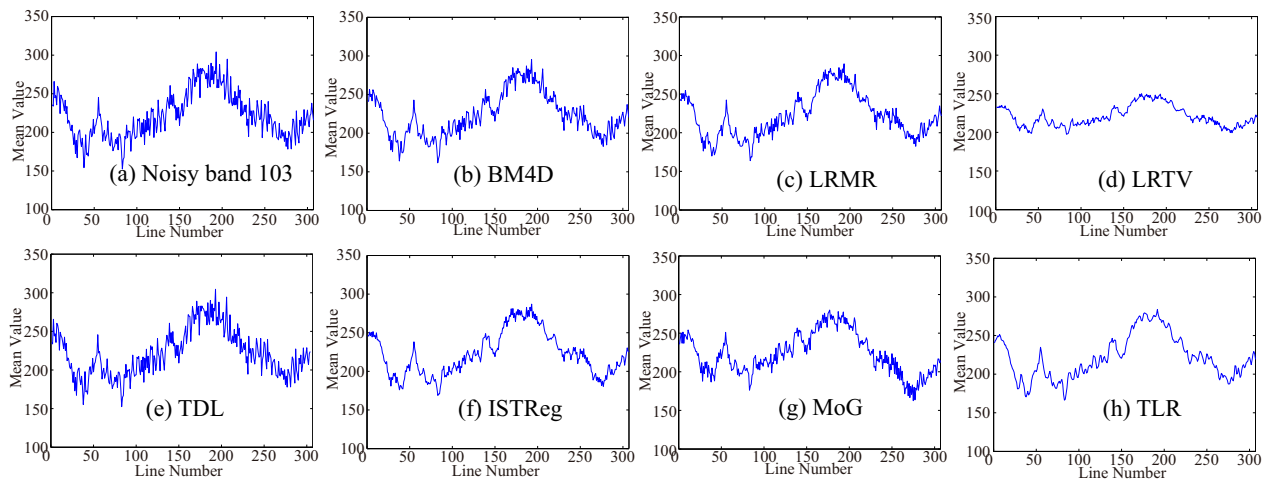


Figure 12. Mean cross-track profiles for images shown in Fig. 11.

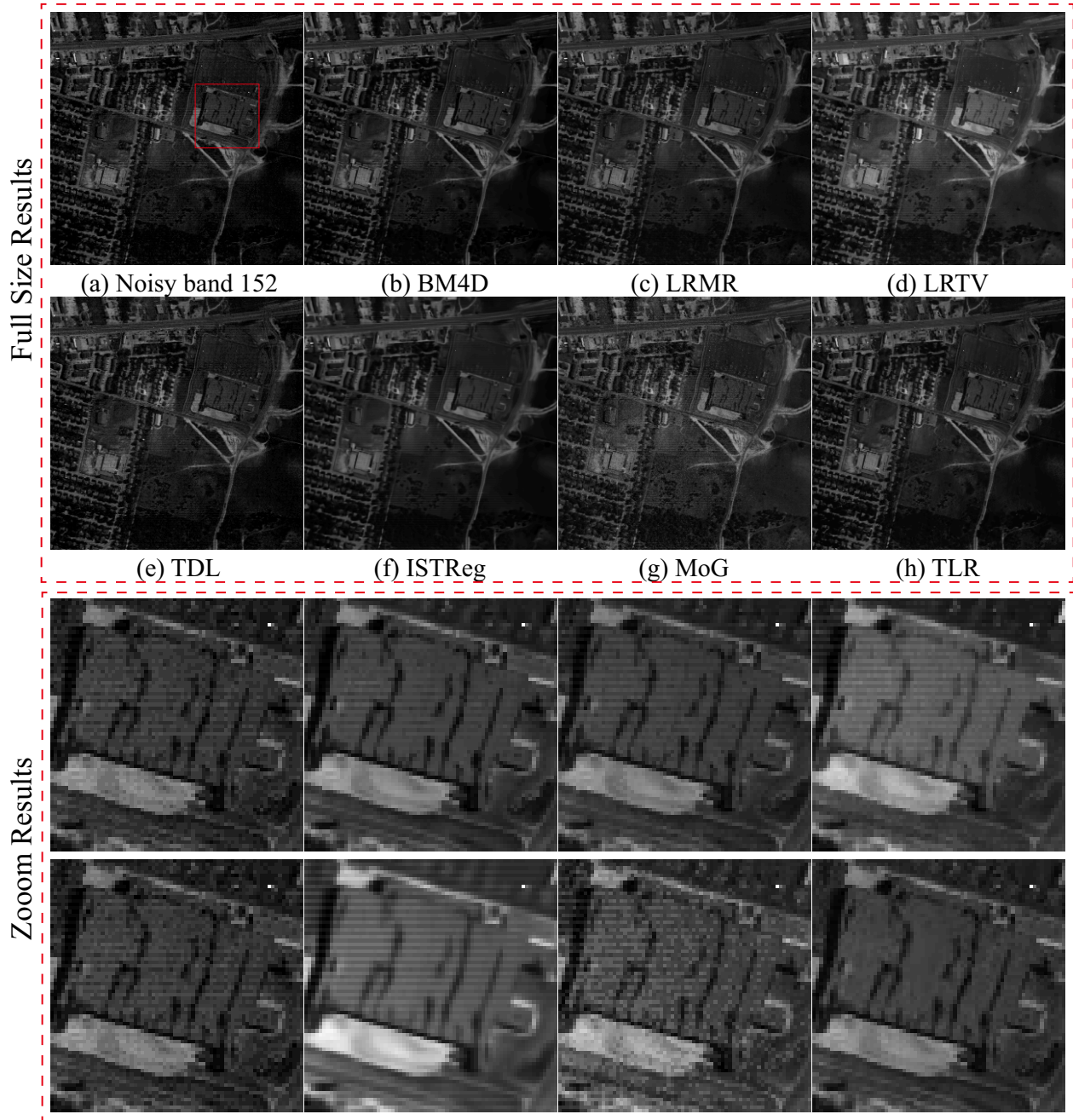


Figure 13. Hypersepctral image *Urban* stripe noise removal results of band 152.

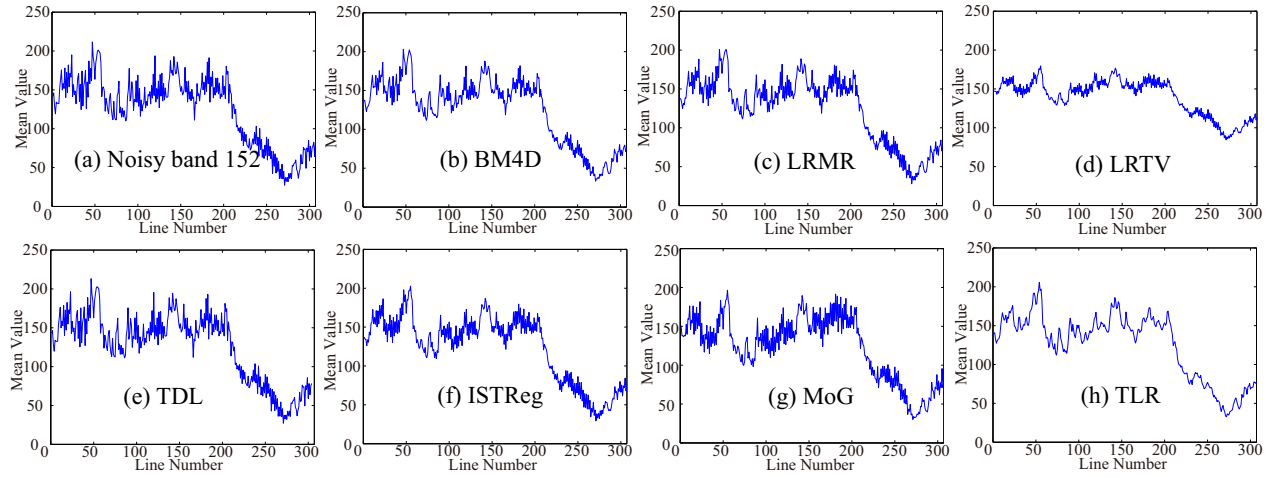


Figure 14. Mean cross-track profiles for images shown in Fig. 13.

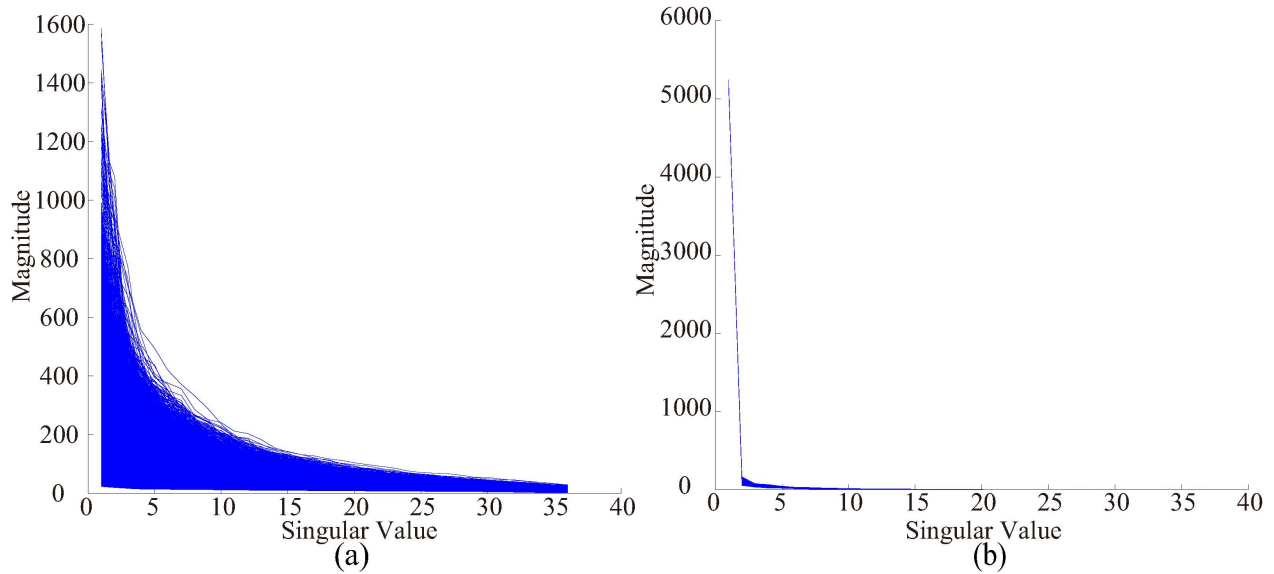


Figure 15. Large scale data low-rank property analysis for both the image and rain component. (a) the image layer, (b) the rain streak layer.